

# Directed Dispersion of Au Based Catalysts at H<sub>2</sub> Reduction Process for Aerobic Oxidation of Benzyl Alcohol

Hanfei Wang<sup>1,2</sup> · Na Liu<sup>1,2</sup> · Chunli Xu<sup>1,2</sup> · Wensheng Dong<sup>1,2</sup> · Chunling Liu<sup>1,2</sup>

Received: 25 August 2016 / Accepted: 28 November 2016 / Published online: 22 December 2016  
© Springer Science+Business Media New York 2016

**Abstract** Controlled synthesis of bimetallic catalysts has attracted much attention in heterogeneous catalysis because their catalytic activity depends on the size of nanoparticles and hence the methods of synthesis. In this work, one convenient method was proposed, with an aim to control the size and dispersion of bimetallic nanoparticles. In this method, Cu<sup>2+</sup> (or Ni<sup>2+</sup>) configurational ion of hydrotalcites was used as directing reagent, which directed the position and dispersion of the final bimetallic nanoparticles by employing the metal interaction between Cu and Au as the driving force. The size, structure and composition of bimetallic nanoparticles were characterized using techniques of X-ray diffraction (XRD), nitrogen physisorption, X-ray photoelectron spectra (XPS) and scanning transmission

electron microscopy (STEM). The mean size of bimetallic AuCu nanoparticles was 2.5 nm, which was 1/4 (Step-impregnation) or 1/10 (Co-impregnation) of that prepared by traditional methods. Even if the loading of Au was increased to 10 wt%, the obtained AuCu nanoparticles were still well dispersed. The catalytic activity of AuCu and AuNi nanoparticles in aerobic oxidation of benzyl alcohol was far higher than those prepared by traditional methods. The mechanism of forming bimetallic nanoparticles was investigated. It was found that the dispersion of Cu<sup>2+</sup> (or Ni<sup>2+</sup>) and the interaction between Cu<sup>0</sup> (or Ni<sup>0</sup>) and Au<sup>0</sup> are two key factors affecting the dispersion of AuCu (or AuNi) nanoparticles.

---

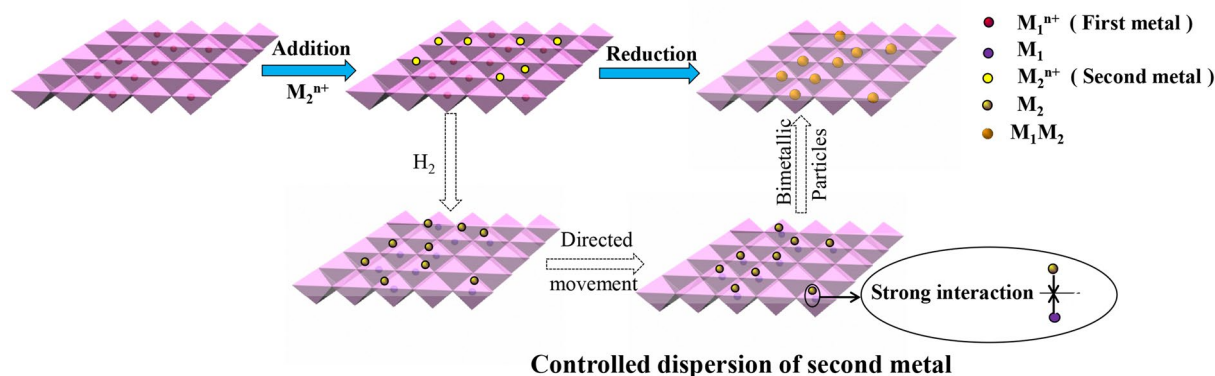
✉ Chunli Xu  
xuchunli@snnu.edu.cn

<sup>1</sup> Key Laboratory of Applied Surface and Colloid Chemistry (Shaanxi Normal University), Ministry of Education, Xi'an 710119, People's Republic of China

<sup>2</sup> School of Chemistry and Chemical Engineering, Shaanxi Normal University, Chang'an West Street 620, Xi'an 710119, People's Republic of China

## Graphical Abstract

## Well dispersion of first metal



**Keywords** Controlled synthesis · Hydrotalcites · AuCu · AuNi · Alcohol oxidation

## 1 Introduction

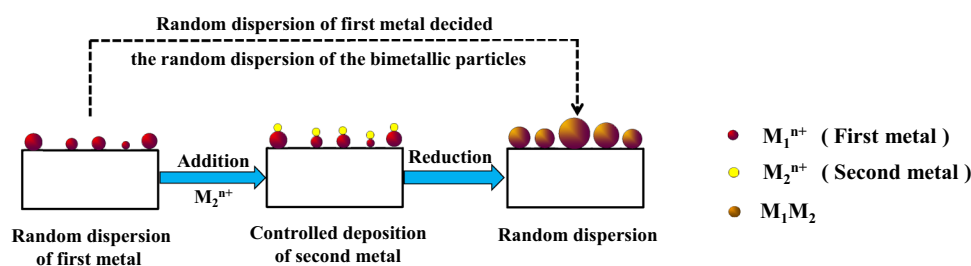
Supported bimetallic catalysts have drawn increasing attention because of their promising in activity enhancement and improved stability in many reactions through forming new active sites and inducing synergistic effects [1, 2]. The catalytic activity of supported bimetallic catalysts is highly dependent on the size of nanoparticles [3, 4]. Generally a particle size less than 3–5 nm with a narrow size distribution and compositional homogeneity are considered to be most beneficial for the catalytic performance [5–8], and the size of nanoparticles is highly dependent on the method of synthesis [4].

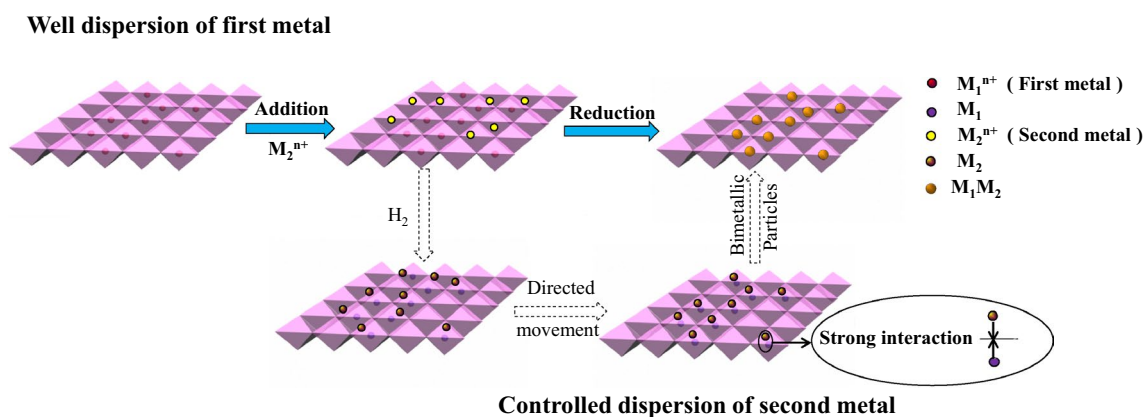
The most traditional synthetic techniques for preparing supported bimetallic catalysts are co-impregnation and deposition–precipitation methods [2, 9, 10]. The two methods are simple, but they can not very well control over the size of metal particle [4]. Various new attempts in the literature were conducted to control the size of bimetallic nanoparticles by improving the conventional methods [4] or developing new methods [11]. Sol immobilization method have been used to control the particle growth by employing

stabilizer–ligands [2, 4]. However, stabilizing polymer usually affects catalytic property of their stabilized nanoparticles and also increases the cost of catalysts [12]. In case industrial applications are targeted, the sol immobilization method is not very attractive due to the use of stabilizer–ligands [13].

In one array of the attempted methods, stepwise deposition of metals was often employed, in which one metal was first added to supports, followed by deposition of second metal (Scheme 1). The deposition of the second metal was controlled by employing a driving force, i.e., the interaction between first metal and second metal. Barbier research group utilized a driving force, i.e., surface redox reactions between second metal and  $H_2$  adsorbed on the pre-existing metal to control the deposition of second metal [14–17]. Besides, other driving forces were also employed, including electroless deposition [13, 18–22], galvanic replacement [23, 24], and complexation [25]. These works demonstrated that the procedure of controlling the deposition of a second metal on the surface of a pre-existing metallic surface are useful in controlling the degree of dispersion of the final bimetallic nanoparticles. They also implied that dispersion of first metal worked as the base of the final bimetallic nanoparticles (Scheme 1). Although the deposition of second metal was controlled in the modified methods shown above, the size of the pre-existing metal was not

**Scheme 1** Schematic of the modified method reported in the literature for preparation of bimetallic nanoparticles

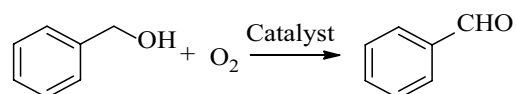




**Scheme 2** Schematic of the proposed method for preparation of bimetallic nanoparticles

very well controlled because of its deposition by employing the conventional impregnation [13, 19, 25] or deposition–precipitation methods [22]. These modified methods have no control over the deposition of first metal, but concentrate on using the dispersion of first metal to control the deposition of second metal. The absence in controlling the dispersion of first metal leads to the deficiency in controlling the dispersion of final bimetal catalysts [26]. It will be deduced that if the size of the pre-existing metal is also well controlled besides the controlled deposition of second metal, bimetallic nanoparticles can be better dispersed.

Inspired by the above deduction, we proposed a new strategy to control the degree of dispersion of the bimetallic nanoparticles by controlling both the degree of dispersion of a pre-existing metal as well as the second metal. As shown in Scheme 2, the first metal as configurational ion was well dispersed in the lattice of supports. The dispersion of second metal was controlled by employing a driving force, i.e., alloy formation between first metal and second metal. Hydrotalcite-like compounds (HTs) are common supports [27–29], here HTs were also employed as supports. HTs are crystalline anionic clays, which are like the naturally occurring brucite (Mg(OH)<sub>2</sub>)-composed of metal hydroxide sheets, where the metal cations are octahedrally coordinated by hydroxide ions [30]. The general formula to describe the chemical composition is [M<sup>II</sup><sub>1-x</sub>M<sup>III</sup><sub>x</sub>(OH)<sub>2</sub>]A<sup>n-</sup><sub>x/n</sub>·mH<sub>2</sub>O, where M<sup>II</sup> and M<sup>III</sup> represent metallic cations, A<sup>n-</sup> indicates the interlayer anion, x is the molar ratio of M<sup>III</sup>/(M<sup>II</sup> + M<sup>III</sup>) and m represents the amount of water. The cations in the layers can be isomorphously substituted by many others, such as Zn, Co, Ni, Mn, Fe (divalents), and Al, Cr, Co, Fe, V, Y, Mn, Ga, lanthanides (trivalents). Herein, we prepared Mg–Al HTs with 2:1 of Mg:Al atomic ratio, wherein Mg<sup>2+</sup> was partially isomorphously substituted by



**Scheme 3** Aerobic oxidation of benzyl alcohol

Cu<sup>2+</sup> or Ni<sup>2+</sup>. And then, HAuCl<sub>4</sub> was deposited on HTs by impregnation. The HAuCl<sub>4</sub>/HTs was reduced by H<sub>2</sub> at the elevated temperature, obtaining well dispersed AuCu or AuNi nanoparticles. The Cu<sup>2+</sup> or Ni<sup>2+</sup>, as configurational ion of HTs, was well dispersed in the lattice of HTs, which decided the highly dispersion of Cu<sup>0</sup> or Ni<sup>0</sup>. Cu<sup>0</sup> or Ni<sup>0</sup> could interact with Au<sup>0</sup> to form the corresponding alloy. Therefore, the well dispersed Cu<sup>0</sup> or Ni<sup>0</sup>, and the metal interaction between Cu<sup>0</sup> (or Ni<sup>0</sup>) and Au<sup>0</sup>, could well control the degree of dispersion of the final AuCu or AuNi nanoparticles. The oxidation of alcohols to their corresponding carbonyl compounds is one of the most important transformations in organic synthesis, and likely play a significant role in the development of value-added chemicals from biomass [31–35]. Recently, Liu et al. prepared Au/Cr-HTs catalysts. The strong synergy between chromium (III)-containing HTs and gold nanoparticles showed higher activity in the aerobic oxidation of alcohols [32]. Very recently, Du et al. [33] designed a flower-like hierarchical Au/NiAl-HTs catalyst, which promoted 60% higher activity than the common Au/NiAl-HTs nanoparticle catalyst in the oxidation of benzyl alcohol. The higher activity of the catalysts could be attributed to the shape selectivity of straight macropores and the synergistic between Ni and Au. Therefore, the development of efficient catalysts, which can aerobically oxidize a variety of alcohols to their corresponding aldehydes and ketones, is of both economic and environmental significance. In

this work, the bimetallic catalyst by the proposed method exhibited good catalytic performance in the aerobic oxidation of benzyl alcohol (Scheme 3).

## 2 Experimental

### 2.1 Preparation of Supports

HTs with desired atomic ratios of  $\text{Cu}^{2+}/\text{Mg}^{2+}/\text{Al}^{3+}$  or  $\text{Ni}^{2+}/\text{Mg}^{2+}/\text{Al}^{3+}$  were prepared by a co-precipitation method as described in our previous report [36]. Typically, a 80 mL aqueous solution ( $\text{Cu}^{2+}$ ,  $\text{Mg}^{2+}$ , and  $\text{Al}^{3+}$ ; or  $\text{Ni}^{2+}$ ,  $\text{Mg}^{2+}$ , and  $\text{Al}^{3+}$ ) with a total concentration of 1.5 M and another 160 mL NaOH aqueous solution (1.5 M) was slowly dropwise added into 50 mL  $\text{Na}_2\text{CO}_3$  aqueous solution under vigorous stirring at room temperature. The molar quantity of  $\text{Na}_2\text{CO}_3$  employed was twice that of  $\text{Al}^{3+}$ . The pH value of the mixture was kept constant, typically at values between 9.5 and 10.5 by adjusting the rate of NaOH aqueous solution. Then, the suspension was aged at 60 °C for 18 h with constant stirring to generate the heavy slurry. The slurry was then cooled down to room temperature, filtered, and washed with water until the pH value of the filtrate was near 8–9. The precipitate was dried at 110 °C overnight. The obtained HTs were denoted as HTs for  $\text{Mg}^{2+}\text{-Al}^{3+}\text{HTs}$ , Cu-HTs for  $\text{Cu}^{2+}\text{-Mg}^{2+}\text{-Al}^{3+}\text{HTs}$ , and Ni-HTs for  $\text{Ni}^{2+}\text{-Mg}^{2+}\text{-Al}^{3+}\text{HTs}$ , respectively. The HTs was further calcined at 600 °C for 3 h in air. The calcined HTs were named Cu-HTO and Ni-HTO, respectively. Unless other special statement, atomic ratio of  $\text{Cu}^{2+}/\text{Mg}^{2+}/\text{Al}^{3+}$  (or  $\text{Ni}^{2+}/\text{Mg}^{2+}/\text{Al}^{3+}$ ) was referred to 0.1:2:1.

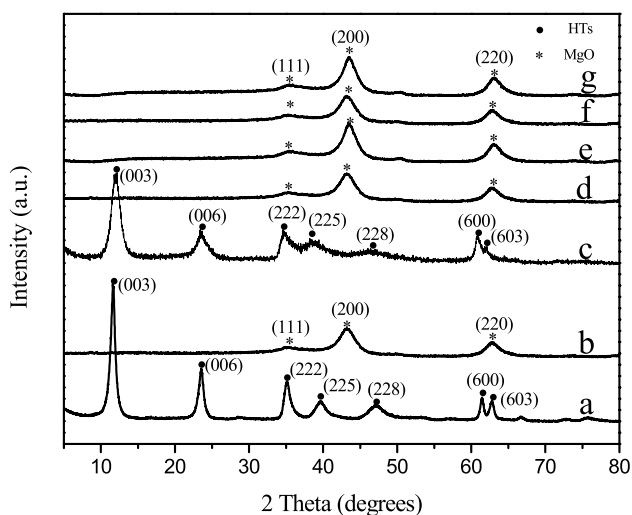


**Fig. 1** XRD patterns of AuCu catalysts and their corresponding supports. *a* Cu-HTs, *b* Cu-HTO, *c* AuCu/HTs-U, *d* AuCu/HTs-300, *e* AuCu/HTO-300, *f* AuCu/HTs-600, and *g* AuCu/HTO-600

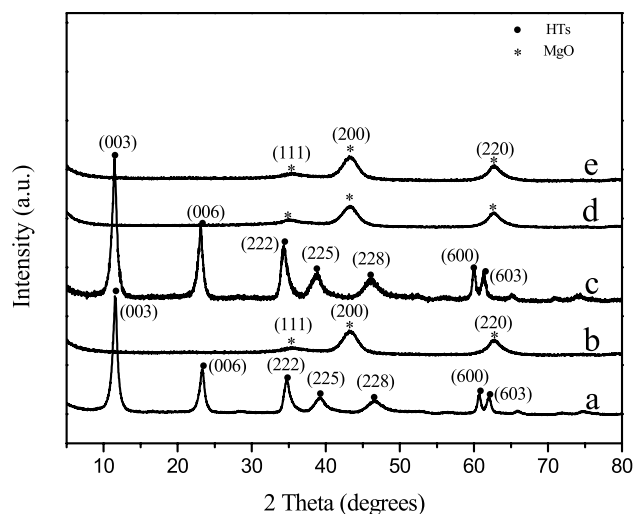


**Fig. 2** XRD patterns of AuNi catalysts and their corresponding supports. *a* Ni-HTs, *b* Ni-HTO, *c* AuNi/HTs-U, *d* AuNi/HTs-600, and *e* AuNi/HTO-600

### 2.2 Preparation of Catalysts

#### 2.2.1 Catalysts Prepared by Proposed Methods

10 mg/mL  $\text{AuCl}_4^-$  solution (AR, 99%, Sinopharm Chemical Reagent Co., Ltd) of desired volume was added to a beaker containing deionized water (15 mL) and supports (1 g) to form slurry. After 2 h of stirring at room temperature, the slurry was quickly dried on hot plate for 0.5 h. The sample after preliminary drying was further dried in

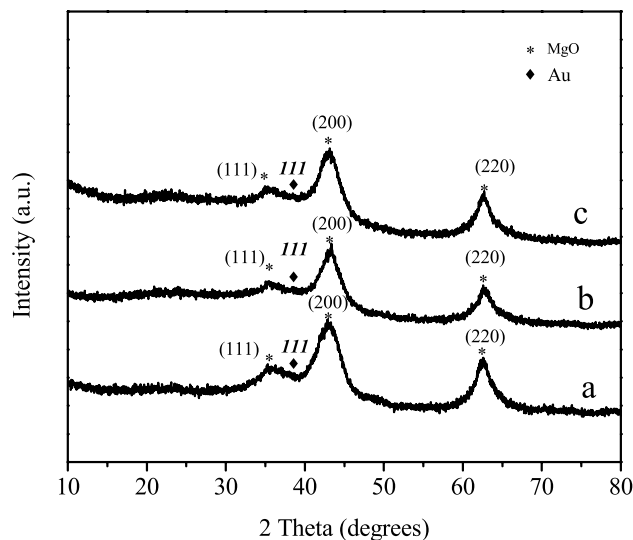


**Fig. 3** XRD patterns of AuCu/HTs-300-C catalysts prepared by traditional methods: *a* Au impregnated before Cu (Stepwise impregnation), *b* Cu impregnated before Au (Stepwise impregnation), and *c* Co-impregnation

**Table 1** Nitrogen physisorption data of supports and catalysts

Entry	Samples	Loading amount of Au (wt%)	BET surface area (m <sup>2</sup> g <sup>-1</sup> ) <sup>a</sup>	Pore volume (cm <sup>3</sup> g <sup>-1</sup> ) <sup>b</sup>	Pore diameter (nm) <sup>b</sup>
1	Cu-HTs	–	141	0.70	16.5
2	Cu-HTO	–	224	1.02	16.7
3	AuCu/HTs-U	1	119	0.72	19.2
4	AuCu/HTs-300	1	163	1.01	20.2
5	AuCu/HTs-300	2	149	0.80	22.9
6	AuCu/HTs-300	2.5	124	0.75	24.2
7	AuCu/HTs-300	3	119	0.65	20.6
8	AuCu/HTs-300	3.5	106	0.60	21.3
9	AuCu/HTs-300	5	104	0.53	26.2
10	AuCu/HTs-300	10	102	0.50	25.6
11	AuCu/HTs-600	1	195	1.11	25.9
12	AuCu/HTO-300	1	120	0.47	7.3
13	AuCu/HTO-600	1	169	0.55	9.3
14	Ni-HTs	–	130	0.57	13.3
15	Ni-HTO	–	270	1.14	13.7
16	AuNi/HTs-U	1	109	0.64	17.5
17	AuNi/HTs-600	1	146	0.89	18.2
18	AuNi/HTO-600	1	126	0.46	8.9
19	HTs	–	118	0.48	11.3
20	Au/HTs-U	1	107	0.77	21.4
21	Au/HTs-300	5	180	0.86	19.2
22	Au/HTs-300	10	104	0.62	23.9

<sup>a</sup>Calculated by the BET method<sup>b</sup>Calculated by the BJH method from the desorption isotherm

oven and air atmosphere at 100 °C for 3 h. The dried samples were reduced by H<sub>2</sub> (30 mL/min) at 300 or 600 °C for 1 h to obtain the final catalysts. The catalysts before reduction was denoted AuM/HTs-U, while the catalysts after reduction were named AuM/HTs-T or AuM/HTO-T, respectively. M was referred to Cu or Ni, U was referred to before reduction, and T was referred to reduction temperature. The samples with HTO meant that the HT supports have been pre-calcined as mentioned in the previous section. Unless other special statement was shown, loading amount of Au was referred to 1 wt% of supports.

### 2.2.2 Catalysts Prepared by Traditional Methods

For comparison, the catalysts were also prepared by traditional methods, such as co-impregnation method and stepwise impregnation method.

The details for co-impregnation method were shown below. A desired volume of HAuCl<sub>4</sub>·4H<sub>2</sub>O solution (10 mg/mL) and Cu(NO<sub>3</sub>)<sub>2</sub>·3H<sub>2</sub>O solution (10 mg/mL) was added simultaneously to a beaker containing deionized water (15 mL) and 1 g of HTs supports to form a slurry. After 2 h of stirring at room temperature, the slurry was quickly

dried on hot plate for 0.5 h. The sample after preliminary drying was further dried in oven and air atmosphere at 100 °C for 3 h. The dried sample was reduced at 300 °C in H<sub>2</sub> for 1 h to obtain final catalyst, denoted as AuCu/HTs-C.

The difference between stepwise impregnation method and co-impregnation method was the adding sequence of metal ions. For sequential impregnation, one ion (Au<sup>3+</sup> or Cu<sup>2+</sup>/Ni<sup>2+</sup>) was first added to HTs supports. After drying, the other ion was added using similar procedure.

### 2.3 Characterization of Catalysts

X-ray diffraction (XRD) patterns were recorded using an X-ray powder diffractometer (Rigaku Co., Japan), and a Cu-Kα Source fitted with an Inel CPS 120 hemispherical detector. The patterns were taken over the 2θ range from 5° to 80°.

The surface area, pore characteristics and average pore diameter of the materials were analyzed with a Micromeritics ASAP 2020 HD 88 instrument. Pore volume and pore size distribution curves were obtained from analysis of desorption branches of the nitrogen isotherms using the BJH method. The samples were degassed at 140 °C for 6 h in

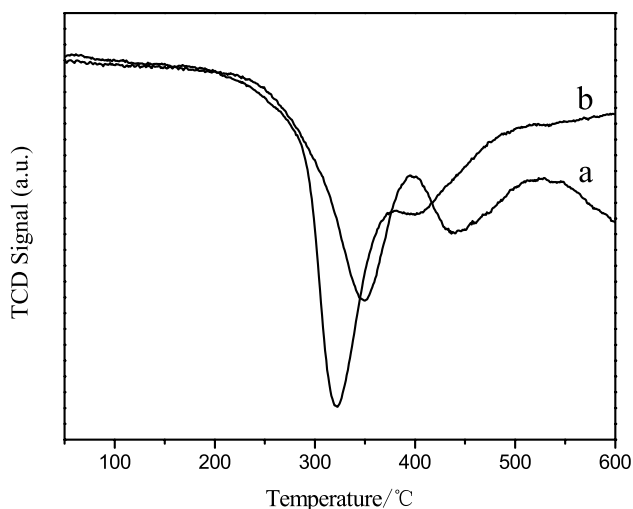


**Fig. 4** H<sub>2</sub>-TPR profiles of *a* Cu-HTs and *b* Cu-HTO

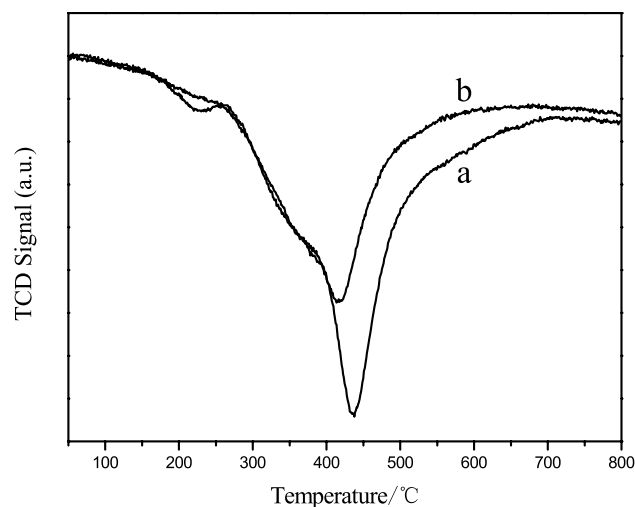


**Fig. 6** H<sub>2</sub>-TPR profiles of *a* Au/HTs-U and *b* Au/HTO-U

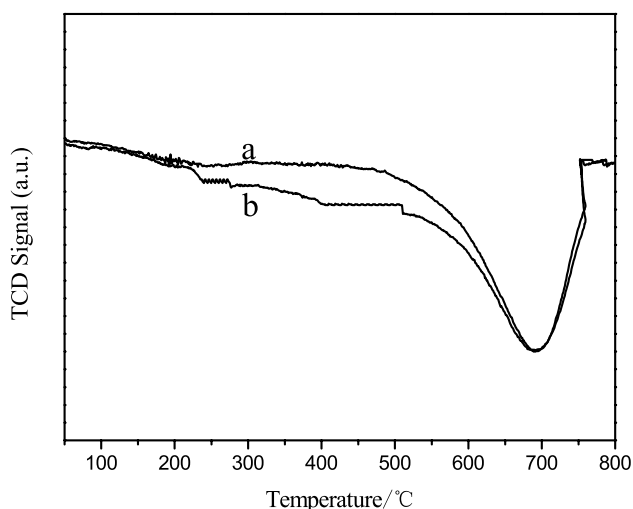


**Fig. 5** H<sub>2</sub>-TPR profiles of *a* Ni-HTs and *b* Ni-HTO

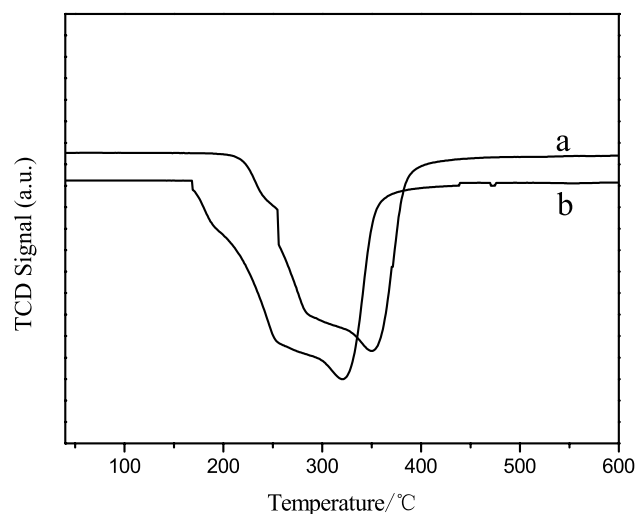


**Fig. 7** H<sub>2</sub>-TPR profiles of *a* AuCu/HTs-U and *b* AuCu/HTO-U

N<sub>2</sub> prior to surface area measurement. Nitrogen adsorption and desorption isotherms were measured at 77 K. Nitrogen adsorption data were obtained in the relative pressure range from 0.06 to 0.30. Total pore volumes were estimated from the amount of nitrogen adsorbed at a relative pressure of 0.995.

H<sub>2</sub>-temperature-programmed reduction (H<sub>2</sub>-TPR) was conducted over a H<sub>2</sub>-TPR instrument (Micromeritics Co. America) with thermal conductivity detector. After degassed in He atmosphere at 200 °C for 1 h, samples of 50 mg were heated at 10 °C/min from 40 to 800 °C in a flow of dry H<sub>2</sub>/Ar mixture (H<sub>2</sub>/Ar, 10/90 vol) at 50 mL/min.

X-ray photoelectron spectra (XPS) were measured to characterize the Cu, Ni, and Au elements valence of catalysts. XPS experiment was carried out using an Axis Ultra spectrometer (Kratos Analytical Ltd., Japan) with Al K $\alpha$  X-ray source (1486.6 eV, 15 kV, 5 mA) at energy of 150 W and ultrahigh vacuum conditions of  $5 \times 10^{-9}$  Torr. Data analysis was performed using Casa XPS software. The electron binding energy (BE) scale of all spectra was calibrated using C 1 s core excitation at 284.8 eV.

The scanning transmission electron microscopy (STEM), higher resolution TEM (HRTEM), EELS elemental mapping observations and energy dispersive X-ray (EDX) were obtained using a FEI Tecnai G2 F20 instrument (USA).

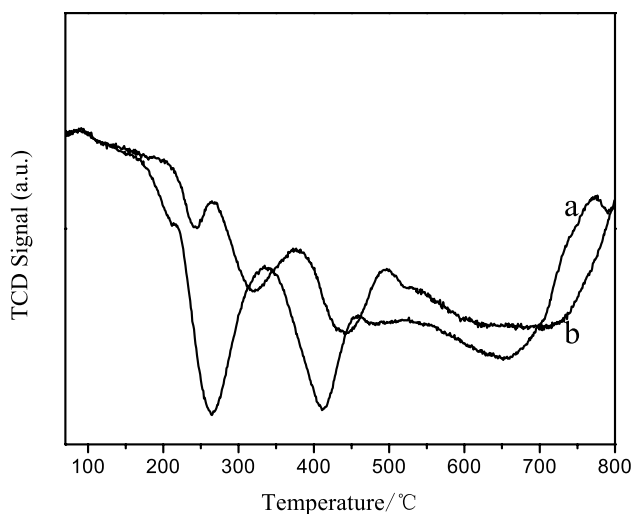


**Fig. 8** H<sub>2</sub>-TPR profiles of *a* AuNi/HTs-U and *b* AuNi/HTO-U

## 2.4 Catalytic Reactions

The aerobic oxidations of benzyl alcohol were carried out using a 50 mL three-necked round-bottle flask equipped with a water-cooled condenser. Typically, the reactor was charged with 0.1 g of catalyst, 1 mmol of benzyl alcohol and 8 mL of toluene at 100 °C for 3 h under an oxygen flow (25–30 mL min<sup>-1</sup>). After cooling to room temperature, N-dodecane (1 mmol), as internal standard, was added. The resulting mixture was diluted to constant volume by toluene in 25 mL volumetric flask. The reaction products were analyzed by using a Shimadzu GC-2014 (Rtx-5 column, 30 m × 0.320 mm, df = 0.25 μm) gas chromatograph equipped with a flame ionization detector.

## 3 Results and Discussion

### 3.1 Catalyst Characterization

#### 3.1.1 XRD Analysis

Figure 1 displays XRD patterns of Cu-HTs, Cu-HTO, and AuCu/HTs before and after reduction. Cu-HTs showed XRD patterns characteristic of HTs [37], with diffraction peak at 11.78°, 23.54°, 34.78°, 39.38°, 46.54°, 60.76° and 62.18° (Fig. 1a). Cu-HTO showed diffraction peaks characteristic of MgO [38], originated from calcination at high temperature (Fig. 1b). The diffraction patterns of AuCu/HTs-U before reduction (Fig. 1c) were similar with that of Cu-HTs (Fig. 1a). This indicated that the impregnation of Au<sup>3+</sup> did not change the structure of HTs supports. The diffraction patterns of AuCu catalysts after reduction (Fig. 1d–g) were similar with that of Cu-HTO (Fig. 1b),

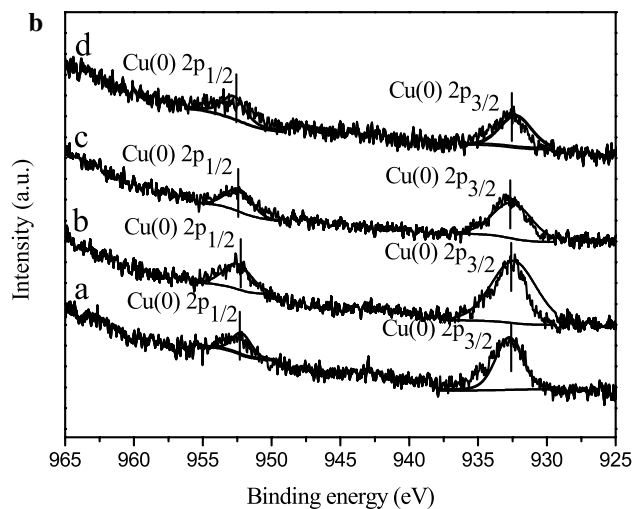
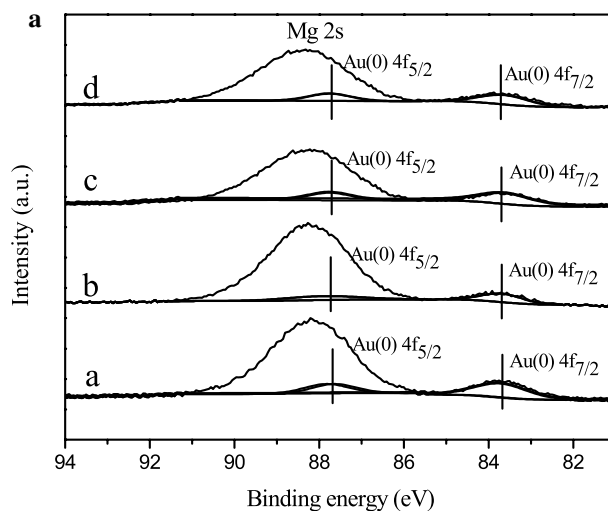


**Fig. 9** Au 4f **a** and Cu 2p **b** XPS spectra of AuCu catalysts. *a* AuCu/HTs-300, *b* AuCu/HTO-300, *c* AuCu/HTs-600, and *d* AuCu/HTO-600

irrespective of the reduction temperature and property of supports. No reflections corresponding to Cu or Au were observed for catalysts because of the low loadings and low size.

Figure 2 displays XRD patterns about Ni-HTs. The effect of calcinations and reduction on structure of Ni-HTs was similar with that of Cu-HTs. The XRD patterns of Ni-HTs and AuNi/HTs-U before reduction (Fig. 2a, c) were similar with that of HTs, while Ni-HTO, AuNi/HTs-600 and AuNi/HTO-600 (Fig. 2b, d, e) showed diffraction peaks similar with that of calcined HTs. XRD patterns of AuCu/HTs-300-C catalysts prepared by traditional co-impregnation and step-impregnation were also determined. As shown in Fig. 3, AuCu/HTs-300-C, irrespective of impregnation method, displayed diffraction patterns characteristic

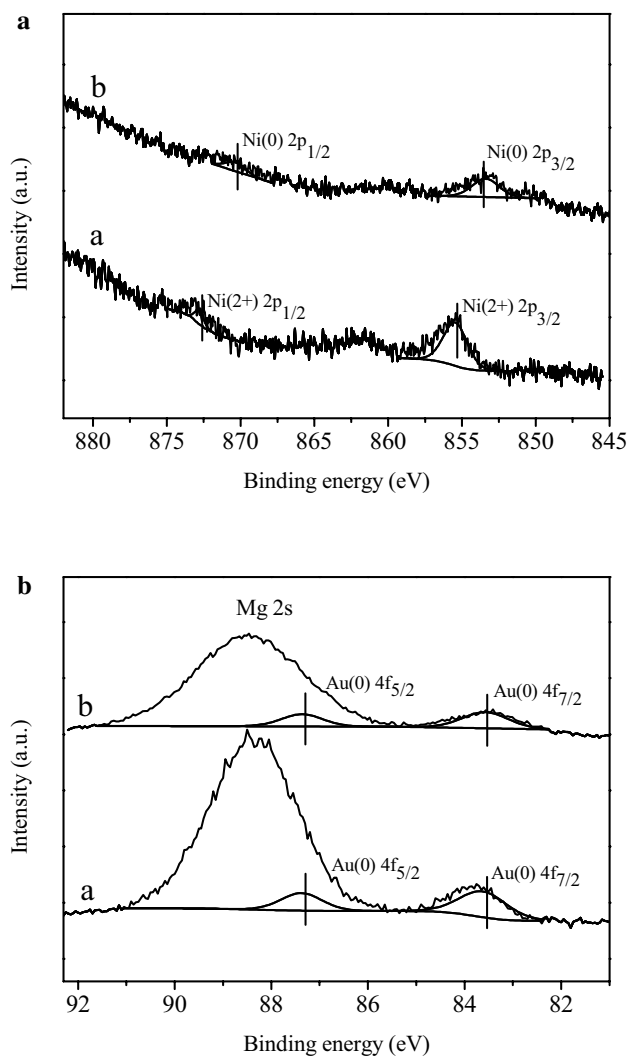


**Fig. 10** XPS spectra in Ni 2p (a) or Au 4f (b) regions of a AuNi/HTs-300 and b AuNi/HTs-600

of MgO, which were similar with that of AuCu/HTs-300. To be worth mentioned, diffraction peaks ascribed to crystalline phase of Au was observed for catalysts prepared by traditional methods (Fig. 3 and Fig. S1). In contrast, no diffraction peaks ascribed to Au was observed for catalysts prepared by this method. This indicated that Au particles size by this work was smaller than that by traditional method.

### 3.1.2 BET Surface Area and Pore Size

HTs and isomorphously substituted HTs had similar surface area, which are in the range of 118–141  $\text{m}^2\text{g}^{-1}$  (Table 1, entries 1, 14, and 19). The calcined HTs displayed higher surface area than that of HTs, which were ascribed to the release of water and  $\text{CO}_2$  during calcinations. The surface of calcined HTs was 224  $\text{m}^2\text{g}^{-1}$  for Cu-HTO

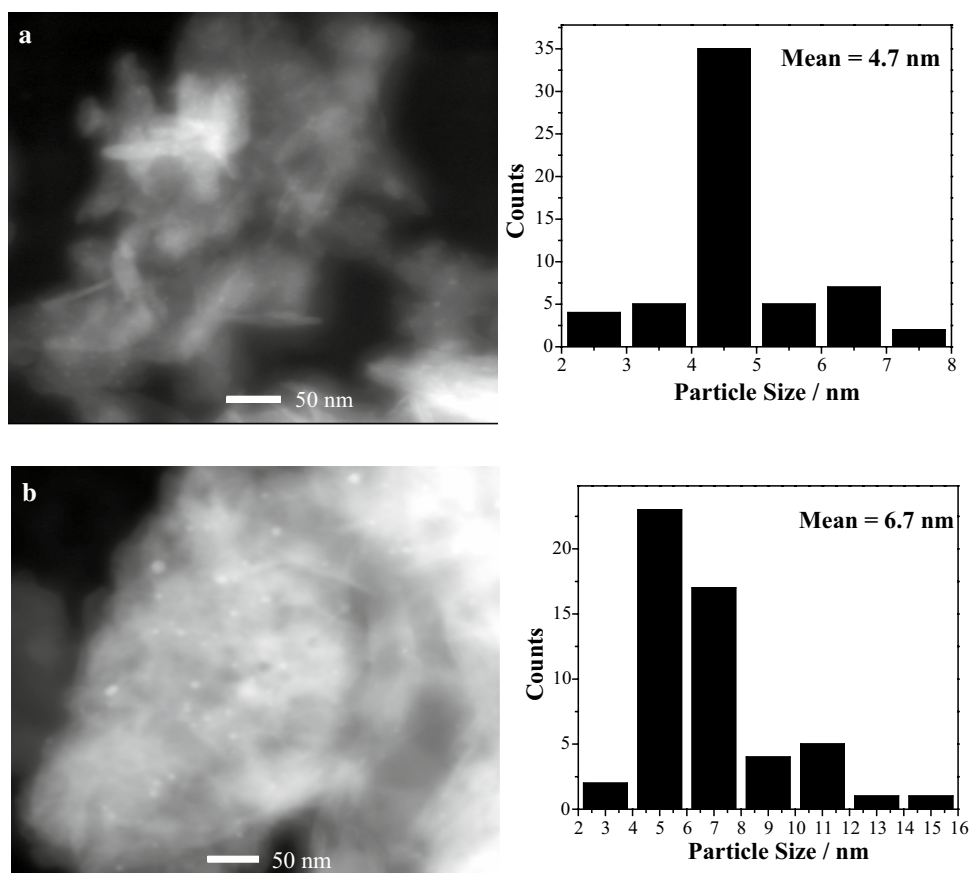
(Entry 2) and 270  $\text{m}^2\text{g}^{-1}$  for Ni-HTO (Entry 15), respectively. After impregnation of Au, the surface area of sample decreased. The surface area of AuCu/HTs-U and AuNi/HTs-U were 119 and 109  $\text{m}^2\text{g}^{-1}$  (Entries 3 and 16), respectively, which was less than their corresponding supports (141 and 130  $\text{m}^2\text{g}^{-1}$ ; entries 1 and 14). The surface area of bimetal catalysts after reduction was higher than that of both catalysts before reduction and intact supports. For example, the surface area of AuCu/HTs-300 (Entry 4) was 163  $\text{m}^2\text{g}^{-1}$ , which was higher than that of AuCu/HTs-U (119  $\text{m}^2\text{g}^{-1}$ , entry 3) and Cu-HTs (141  $\text{m}^2\text{g}^{-1}$ , entry 1). With the increase of Au loading amount, the surface area of AuCu/HTs-300 decreased. It went down to 102  $\text{m}^2\text{g}^{-1}$  when the loading amount was 10 wt% (Entry 10). Furthermore, reduction temperature also affected surface area of catalysts. The surface area of AuCu/HTs-600 was higher than that of AuCu/HTs-300. Its surface area (Entry 11) was 195  $\text{m}^2\text{g}^{-1}$ , which was less than that of AuCu/HTs-300 (163  $\text{m}^2\text{g}^{-1}$ , entry 4). Besides, mean pore diameter of all samples were in the range of 7.3–26 nm. This indicated that all the catalysts were mesoporous. The pore size distributions are shown in the supporting information (Fig. S2). The results showed that the catalysts contained a large amount of mesopores and a small amount of micropores after thermal treatment.

### 3.1.3 $\text{H}_2$ -TPR Analysis

Figure 4 shows TPR profiles for Cu-HTs and Cu-HTO. Both of them displayed one major reduction peak and one minor reduction peak. Cu-HTs showed one major peak centered at around 348 °C and one minor peak around 433 °C. The reduction peak of Cu-HTO shifted to lower temperature, which centered at 318 °C (major peak) and 398 °C (minor peak), respectively. As shown in Fig. 5, TPR curves of Ni-HTs and Ni-HTO exhibited only one reduction peak centered at 690 °C. TPR profiles for supported Au also showed one reduction peak (Fig. 6), which located around 437 °C for Au/HTs-U and 416 °C for Au/HTO-U, respectively. TPR patterns for supported AuCu displayed one broad peak from 214 to 420 °C for AuCu/HTs-U, and from 168 to 367 °C for AuCu/HTO-U (Fig. 7). The broad peak may correspond to the reduction of  $\text{Cu}^{2+}$  to  $\text{Cu}^0$ , and  $\text{Au}^{3+}$  to  $\text{Au}^0$  [39]. It is clear that Cu on the AuCu/HTs catalyst lowered the reduction temperature of  $\text{Au}^{3+}$ . TPR patterns for supported AuNi contain more reduction peaks than that of AuCu catalysts (Fig. 8). Curves of AuNi/HTs-U displayed two sharp peaks located at 266 °C and 414 °C, and one broad peak around 654 °C. Profiles of AuNi/HTO-U displayed three sharp peaks located at 247, 315, and 443 °C, respectively, as well as one broad peak around 717 °C. Compared with HTs supported catalysts, the reduction peak of HTO samples started at lower temperature. For



**Fig. 11** STEM images for **a** Cu-HTs-300 and **b** Cu-HTs-600



example, AuCu/HTO started at 168 °C, which was 36 °C lower than that of AuCu/HTs (Fig. 7). The difference in the reduction peak between HTs and HTO may be ascribed to their difference in metal dispersion, since dispersion affects reduction temperature of elements [40]. The difference in the dispersion between HTs and HTO may be due to calcination because calcination may result in sinter of nanoparticles [41].

#### 3.1.4 XPS Analysis

Figure 9 shows Au 4f and Cu 2p XPS spectra of AuCu/HTs-300, AuCu/HTO-300, AuCu/HTs-600, and AuCu/HTO-600. XPS spectra of Au 4f region for all the samples could be fitted with maximum peaks at 87.4 and 83.8 eV binding energies, which are characteristic of Au<sup>0</sup>. No Au 4f spectra ascribed to Au<sup>δ+</sup> was observed, indicating that Au<sup>3+</sup> was completely reduced to Au<sup>0</sup>. XPS spectra of Cu 2p for all the samples exhibited characteristic peaks of metallic Cu. No Cu<sup>δ+</sup> was detected, suggesting that Cu also had been reduced completely.

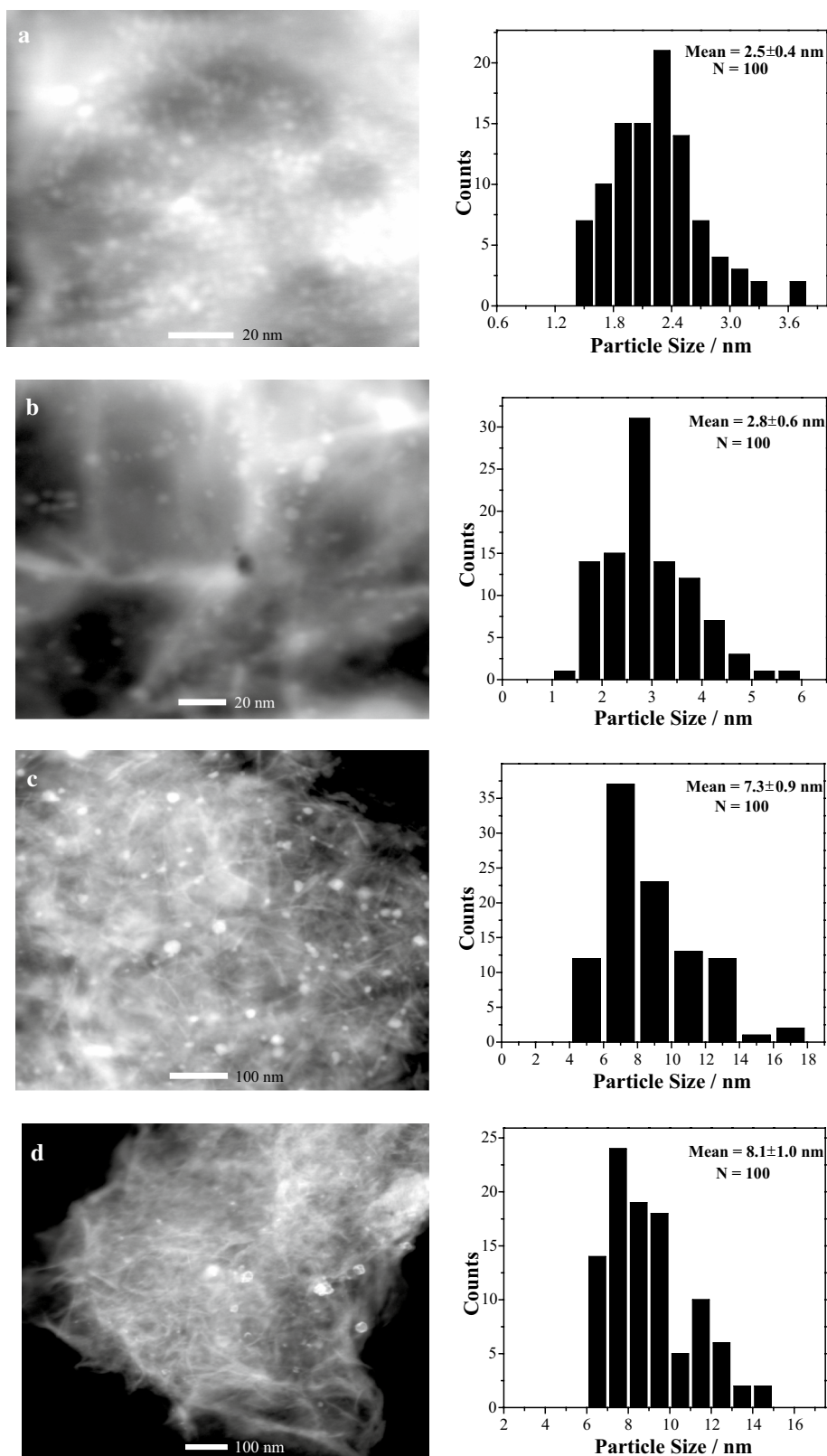
Ni 2p and Au 4f XPS spectra of AuNi/HTs-300 and AuNi/HTs-600 are shown in Fig. 10. Ni 2p XPS spectra of AuNi catalysts varied with reduction temperature. AuNi/HTs-300 exhibited maximum peak at 872 and 855 eV

binding energies, which are characteristic of Ni<sup>2+</sup>, while AuNi/HTs-600 presented maximum peak characteristic of Ni<sup>0</sup>. In the case of Au 4f XPS spectra, both AuNi/HTs-300 and AuNi/HTs-600 showed maximum peaks at 87.4 and 83.8 eV binding energies, which are characteristic of Au<sup>0</sup>. This indicated that metal Ni on AuNi/HTs could not be reduced at 300 °C, and the reduction could be completed at 600 °C. This result was in accordance with that of H<sub>2</sub>-TPR.

#### 3.1.5 STEM Analysis of Supports and Catalysts

**3.1.5.1 Mean Size of Bimetallic Nanoparticles** Figure 11 shows STEM images for Cu-HTs-300 and Cu-HTs-600. The size of Cu nanoparticles was 4.7 nm when reduced at 300 °C. When reduced at 600 °C, the size of Cu nanoparticles was increased to 6.7 nm. This indicated that reduction temperature affected the dispersion of Cu nanoparticles. After impregnation of Au, the formed AuCu nanoparticles were observed. As shown in Fig. 12, AuCu/HTs-300 and AuCu/HTO-300 nanoparticles were well distributed. Their mean size was 2.5 nm and 2.8 nm, respectively. In contrast, AuCu/HTs-600 and AuCu/HTO-600 displayed higher size, which were 7.3 nm and 8.1 nm, respectively. The high size of the latter two AuCu catalysts may be due to the effect of calcinations temperature since they were reduced at 600 °C.

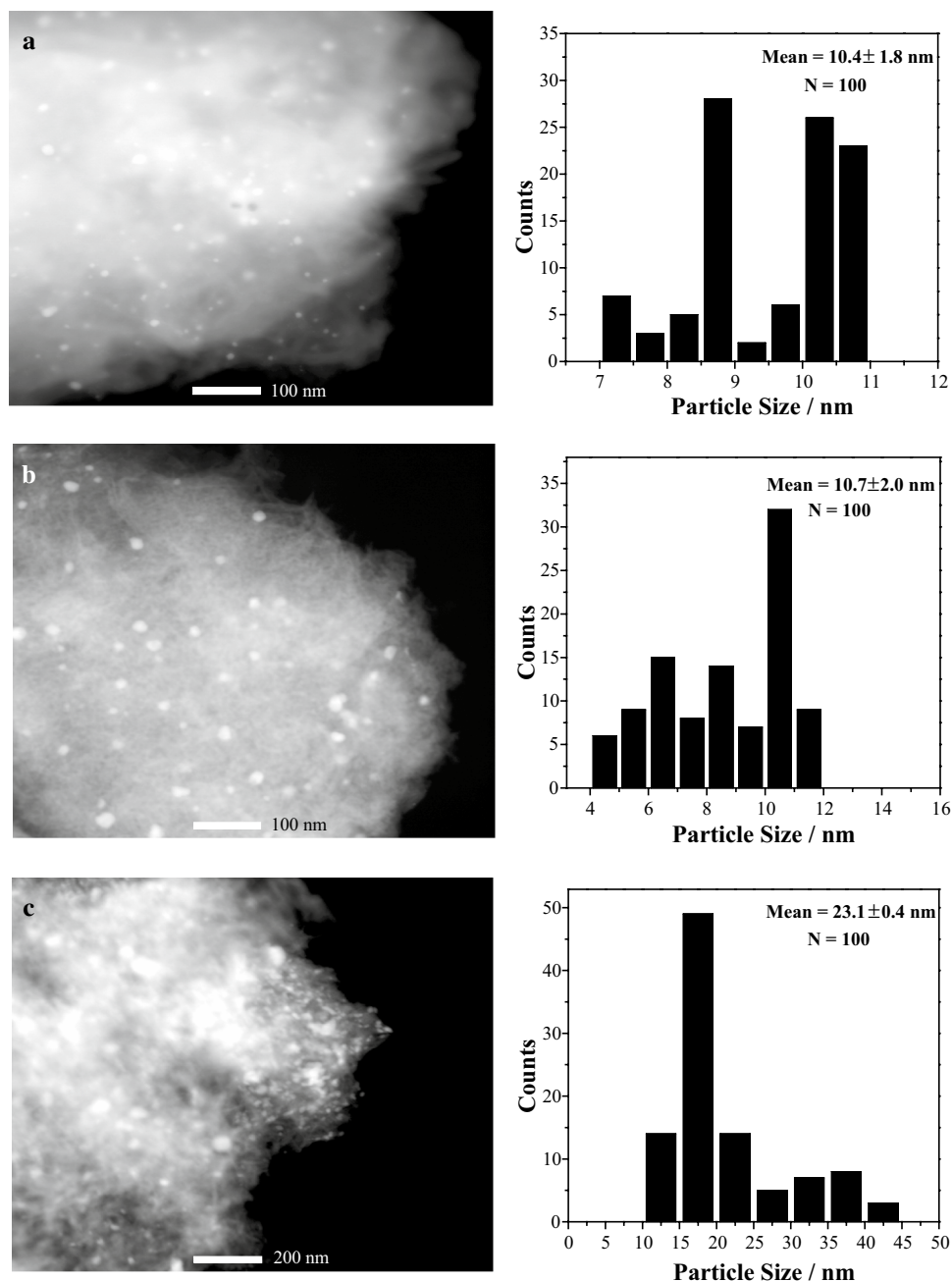
**Fig. 12** STEM images and metal particle size distributions for AuCu catalysts. **a** AuCu/HTs-300, **b** AuCu/HTO-300, **c** AuCu/HTs-600, and **d** AuCu/HTO-600



Effect of Au loading amount was also investigated. As shown in Fig. S3 (Supporting information), AuCu nanoparticles had narrow size distribution in the investigated scope

of loading amount although their size increased slowly with loading amount. The mean size was 2.7 nm for 2 wt% loading (Fig. S3a) and 2.9 nm for 2.5 wt% loading (Fig. S3b).

**Fig. 13** STEM images and metal particle size distributions for AuCu/HTs-300-C catalysts by traditional methods. **a** Au impregnated before Cu, **b** Cu impregnated before Au, and **c** Co-impregnation of Cu and Au

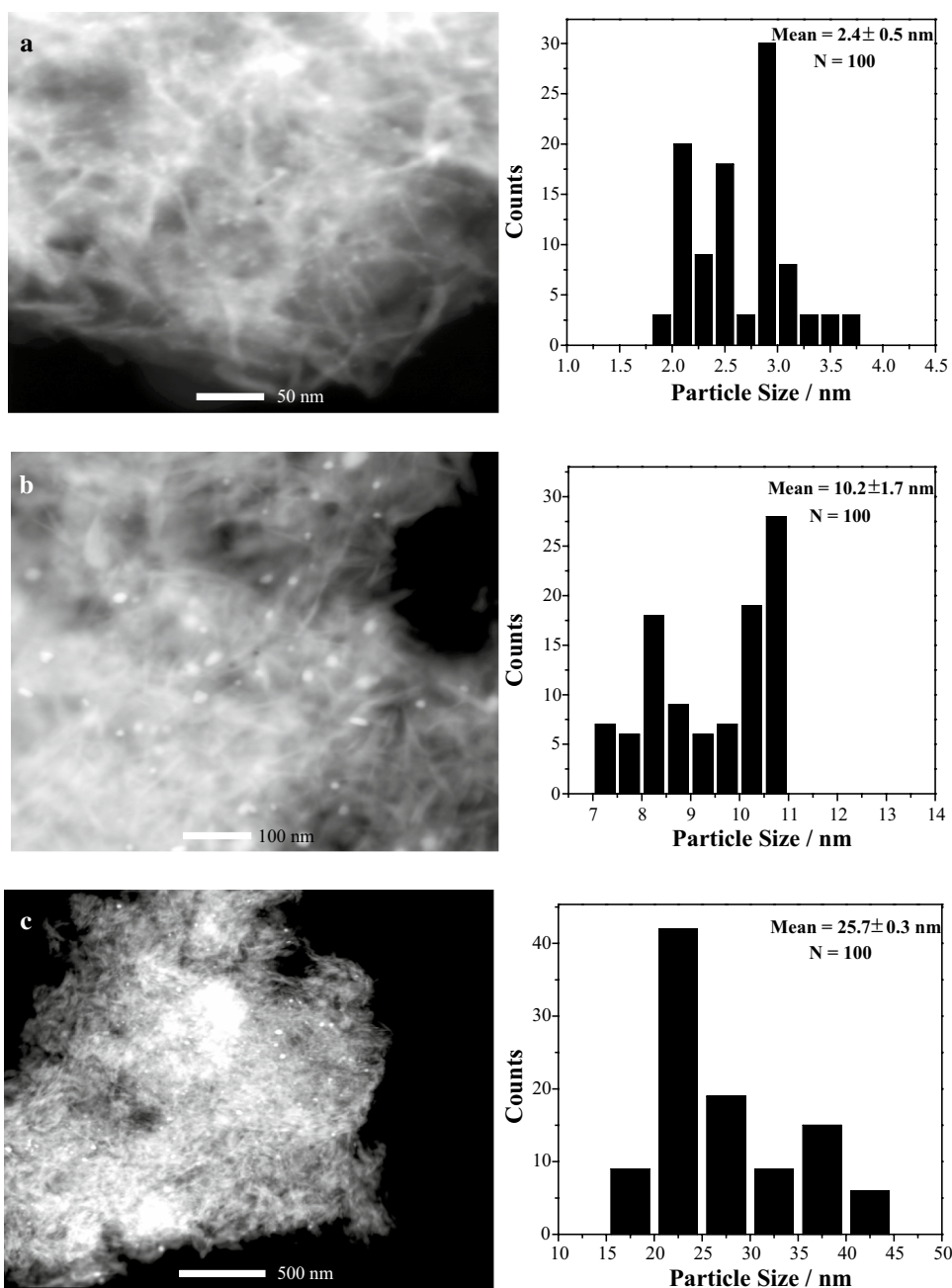


Those sizes were slightly higher than 2.5 nm of AuCu/HTs-300 with 1 wt% loading (Fig. 12a). It rose to 4.6 nm when loading amount was increased to 10 wt% (Fig. S3f). For comparison, AuCu was also prepared using traditional methods. As shown in Fig. 13, the mean size of AuCu by co-impregnation was higher than that by sequential impregnation. The former was around 23.1 nm, while the latter was 10 nm. Compared with those prepared by the proposed method, AuCu nanoparticles by traditional work showed far higher size whether the used method was co-impregnation or sequential impregnation. For the same amount of Au loading, the size of AuCu/HTs-300-C (10.4~10.7 nm,

Fig. 13a and b) by sequential impregnation was four times higher than that of AuCu/HTs-300 by this work (2.5 nm, Fig. 12a). The size of AuCu/HTs-300-C (23.1 nm, Fig. 13c) by co-impregnation was almost 10 times higher than that of AuCu/HTs-300 by this work (2.5 nm, Fig. 12a).

Effect of Cu content was investigated. As shown in Fig. 14a, when Cu:Mg:Al molar ratio was 0.05:2:1, the obtained size of AuCu nanoparticles was 2.4 nm, which was similar with that for 0.1:2:1 (Fig. 12a). When the molar ratio was above 0.1:2:1, the mean size was increased. It went up to 10.2 nm for 0.5:2:1 and 25.7 nm

**Fig. 14** STEM images and metal particle size distributions of AuCu/HTs-300 versus Cu:Mg:Al molar ratio. **a** 0.05:2:1, **b** 0.5:2:1, and **c** 1:2:1



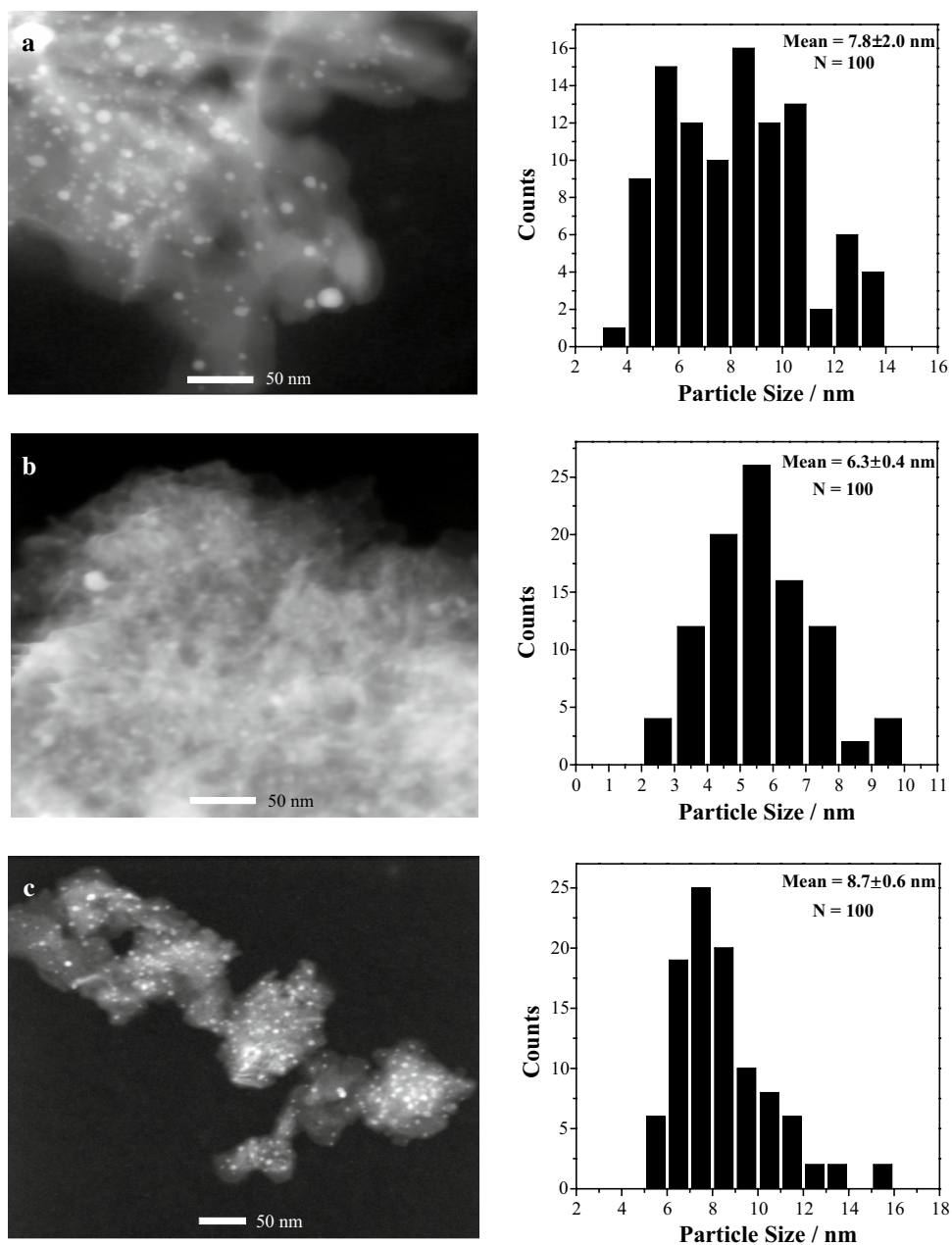
for 1:2:1 molar ratio. This indicated that Cu amount affected the size of AuCu nanoparticles.

The mean size of AuNi catalysts was also determined. As shown in Fig. 15, the mean size of AuNi/HTs-300 was 7.8 nm, which slightly decreased to 6.3 nm (i.e. AuNi/HTs-600) when reduction temperature was increased to 600 °C. The mean size of AuNi/HTs-600-C, i.e., the AuNi catalysts by traditional method, was 8.7 nm, which was slightly higher than that of AuNi/HTs-600 by traditional method. It was obvious that the property in size of AuNi catalysts was different from that of AuCu catalysts. The size of AuNi reduced at 600 °C was smaller than that at 300 °C, while

contrary phenomenon was observed for AuCu catalysts. Besides, the mean size of AuCu catalysts by this work was far smaller than that by traditional work, however, the discrepancy between this work and traditional work was small for AuNi catalysts. The mechanism for the specialty of AuNi catalysts was discussed in the section about mechanism.

**3.1.5.2 Composition of AuCu Nanoparticles** The microstructure and compositions of AuCu nanoparticles were characterized by a STEM with EDS. As shown in Fig. 16, the EDS line scan analysis indicated the nanoparticles were

**Fig. 15** STEM images and metal particle size distributions for AuNi catalysts. **a** AuNi/HTs-300, **b** AuNi/HTs-600, and **c** AuNi/HTs-600-C



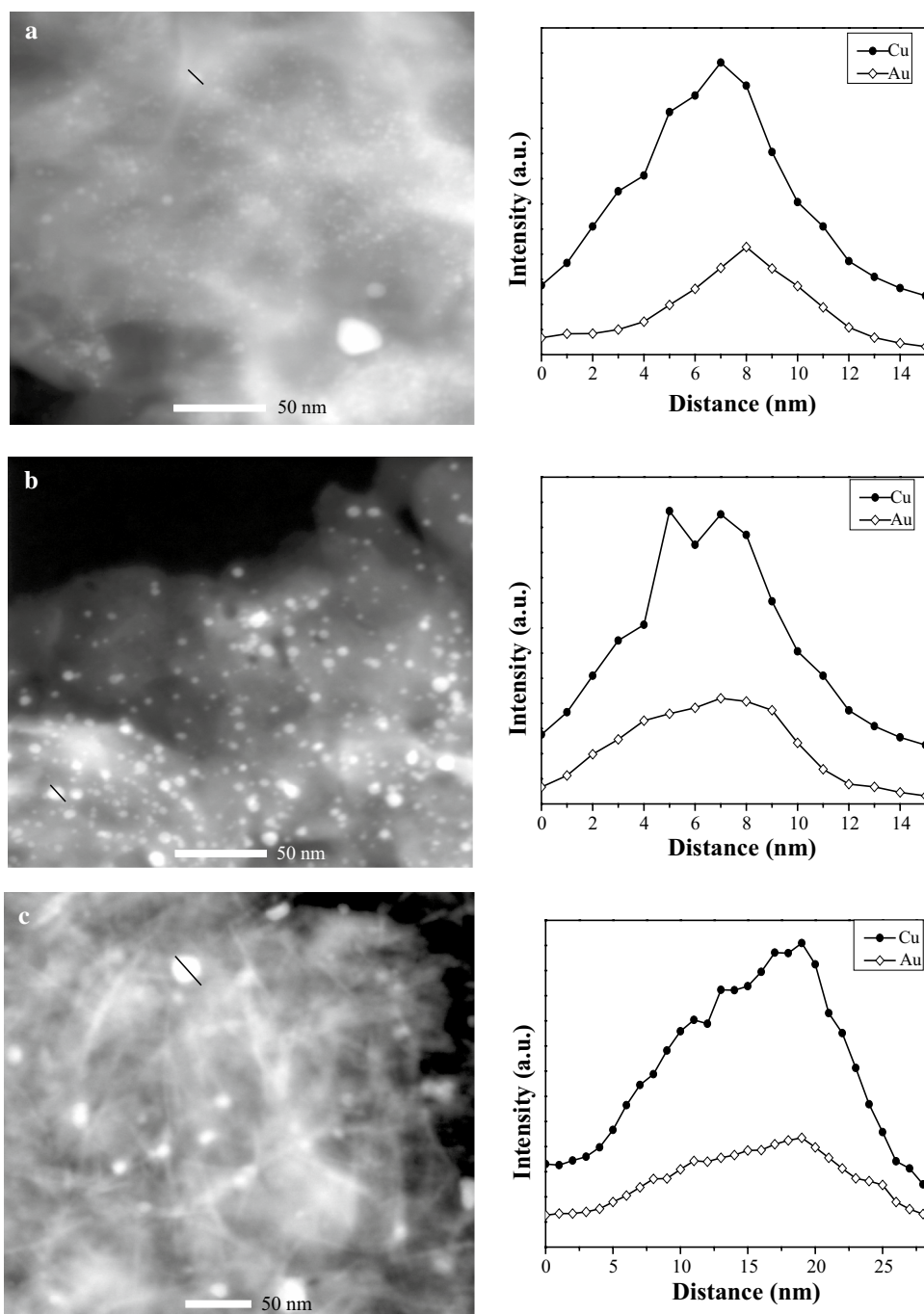
homogeneously AuCu mixed structure irrespective of loading amount and reduction temperature. The EDX mapping images of a selected nanoparticle on the surface of AuCu/HTs-600 were also determined (Fig. 17). The mapping images further confirmed that Au and Cu mixed homogeneously. The homogeneous structure of AuCu bimetallic nanoparticles indicated that there was one kind of interaction between Cu and Au which resulted in their mixture, since Cu and Au was added to supports stepwise. In thermodynamics, the process of forming alloy between Cu and Au is spontaneous [41]. Therefore, it is possible that the interaction is the force of forming alloy. In order to verify the inference, HRTEM was carried out to further reveal the

microstructure of the nanoparticles. As shown in Fig. 18, the interplanar spacing of nanoparticles was 2.12 Å for AuCu/HTs-300 and 2.19 Å for AuCu/HTs-600, which was between 2.09 Å (Cu<sub>111</sub>) and 2.35 Å (Au<sub>111</sub>). This indicates that Au and Cu mixed homogeneously and formed the structure of alloy.

### 3.2 Mechanism Forming Bimetallic Nanoparticles and Factors Affecting the Dispersion of AuCu Nanoparticles

Based on analysis of XRD, XPS, TPR, and STEM, the mechanism to prepare bimetallic nanoparticles was

**Fig. 16** STEM images (*left*) and intensity profiles (*right*) of Cu (M) and Au (M) components in the nanoparticles obtained by a EDS line scan analysis (along the *dark line* in the corresponding STEM images from *left* to *right*). **a** 1 wt% AuCu/HTs-300, **b** 5 wt% AuCu/HTs-300, and **c** 1 wt% AuCu/HTs-600

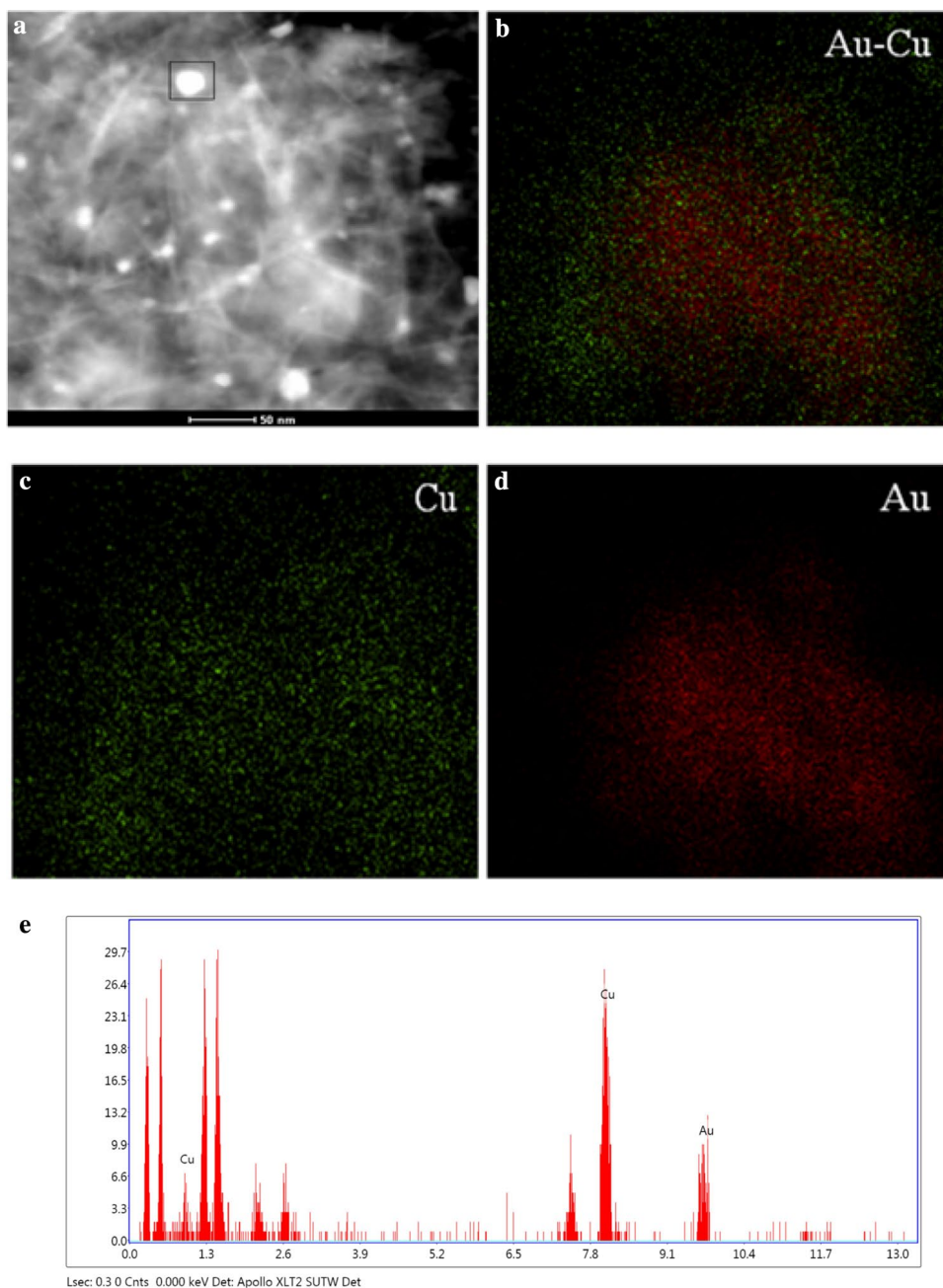


proposed, as shown in Scheme 2. The dispersion of  $\text{Cu}^{2+}$  as configurational ion of HTs, which isomorphously substituted for  $\text{Mg}^{2+}$  in the crystal lattice of HTs, could be well controlled by adjusting its contents in HTs. After impregnation,  $\text{Au}^{3+}$  was randomly deposited on the surface of HTs supports. Upon reduction, there is one kind of interaction, i.e., interaction between  $\text{Cu}^0$  and  $\text{Au}^0$ . The interaction drove  $\text{Au}^0$  to the position of  $\text{Cu}^0$  and hereafter formed alloy. Thereafter, configurational ion  $\text{Cu}^{2+}$  of HTs directed the position of the final AuCu nanoparticles on the surface of

HTs supports. Accordingly, the dispersion of  $\text{Cu}^{2+}$  decided the dispersion of the final AuCu nanoparticles. The direction was realized by the interaction between  $\text{Cu}^0$  and  $\text{Au}^0$ . Hence, dispersion of  $\text{Cu}^{2+}$  and the interaction between  $\text{Cu}^0$  and  $\text{Au}^0$  are two key factors affecting the dispersion of AuCu nanoparticles.

Dispersion of  $\text{Cu}^{2+}$  could be tuned by adjusting its contents in the HTs supports. The change in dispersion of  $\text{Cu}^{2+}$  could affect the dispersion of the final AuCu nanoparticles. That is,  $\text{Cu}^{2+}$  amount affect the dispersion of the final

**Fig. 17** STEM-EDS profile of AuCu/HTs-600. **a** STEM images of AuCu/HTs-600, **b–d** EDX mapping images of a selected nanoparticle (in the *square* of **a**): **b** Au and Cu bimetallic composition, **c** Cu signals, **d** Au signals, **e** EDS spectra of the catalyst

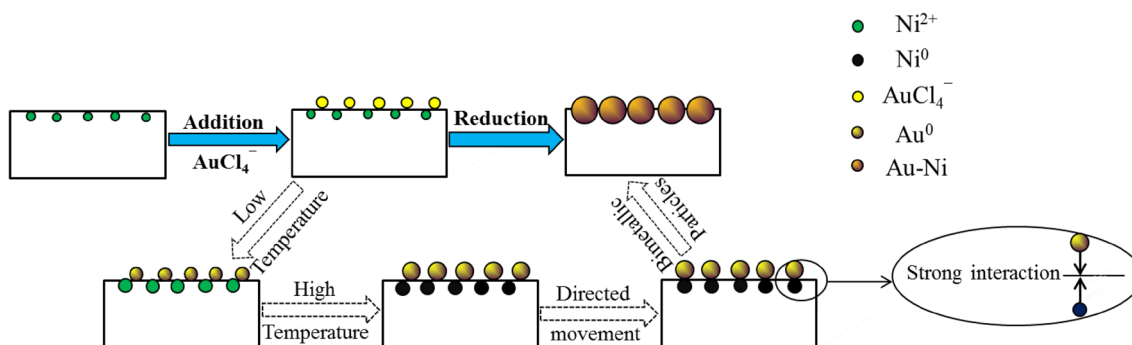
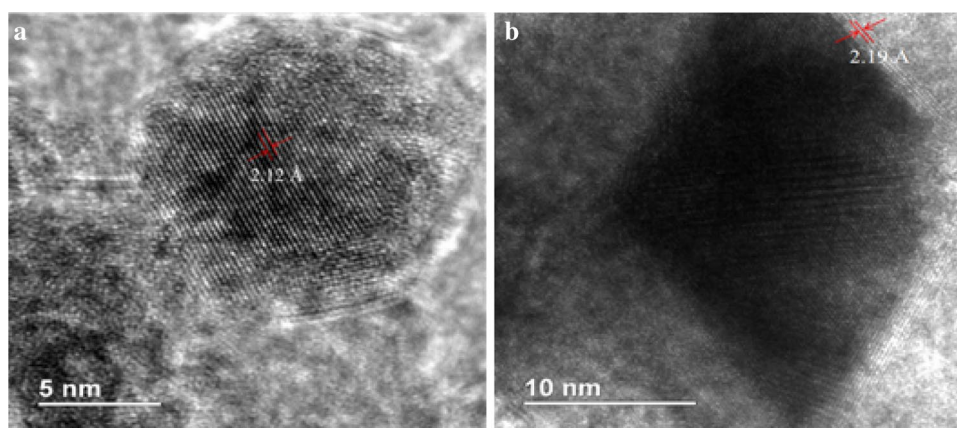


AuCu nanoparticles. As shown in Fig. 14, it was found that Cu amount affected the size of AuCu nanoparticles. These experimental results verified our deduction.

The interaction between Cu<sup>0</sup> and Au<sup>0</sup> could be tuned by controlling the reduction temperature of catalysts. The appropriate reduction temperature for each bimetallic ion should be near each other. TPR analysis showed that the appropriate reduction temperature for Cu<sup>2+</sup> and Au<sup>3+</sup> was near other, which corresponded to the low size of AuCu/HTs-300. If the discrepancy between reduction

temperatures of two metals was too large, dispersion of configurational ion, i.e., the first metal, and the interaction between first metal and Au<sup>0</sup> could not play their role in directing the position and dispersion of the targeted bimetallic nanoparticles (Scheme 4). As shown in Figs. 5 and 6, there is a big discrepancy in the optimum reduction temperature between single Ni and single Au. The XPS spectra for AuNi bimetal in Fig. 10 showed that the reduction of Au<sup>3+</sup> was completed at 300 °C, while none Ni<sup>2+</sup> was reduced at 300 °C, and Ni<sup>2+</sup> was completely reduced at 600 °C. The

**Fig. 18** HRTEM image of **a** AuCu/HTs-300 and **b** AuCu/HTs-600



**Scheme 4** Schematic representation of the controlled synthesis approach for an AuNi bimetallic catalyst

discrepancy in the reduction temperature could explain the property of AuNi/HTs (Fig. 15) reduced at 300 °C and 600 °C, respectively. The nanoparticles of AuNi/HTs-300 had a broader distribution than that of AuNi/HTs-600. As shown in Scheme 4, at 300 °C, the interaction between  $\text{Ni}^0$  and  $\text{Au}^0$  was weak since the reductive degree of  $\text{Ni}^{2+}$  was low. Consequently, the dispersion of  $\text{Ni}^{2+}$  and the interaction between  $\text{Ni}^0$  and  $\text{Au}^0$  did not play their role well in directing the position and dispersion of AuNi nanoparticles. At 600 °C,  $\text{Ni}^{2+}$  was completely reduced, so the metal interaction was increased. This explained the reason of the lower size and narrower distribution of AuNi/HTs-600. However, the size of AuNi/HTs-600 was bigger than that of AuCu/HTs-300 although alloying force did work. The higher in the size of AuNi/HTs-600 was due to the increased size of Au nanoparticles. Before  $\text{Ni}^{2+}$  was completely reduced and metal interaction between Au and Ni did not work, the single Au nanoparticles were already sintered because of the increased reduction temperature.

Besides guaranteeing the complete reduction of every bimetallic ion, appropriate reduction temperature could avoid the sinter of bimetallic nanoparticles. If reduction

temperature was set above the appropriate reduction temperature, bimetallic nanoparticles would sinter although bimetallic ions could be completely reduced. As shown in Fig. 12, 300 °C was appropriate reduction temperature for AuCu bimetal, while 600 °C was highly above 300 °C and led to the sinter of the bimetallic nanoparticles.

In order to verify the mechanism shown above, AuCuNi/HTs-600 was prepared (Fig. 19). The size of AuCuNi/HTs-600 was 2.1 nm and similar or even smaller than that of AuCu/HTs-300, which was far smaller than that of both AuCu/HTs-600 and AuNi/HTs-600. This indicated that AuCuNi/HTs-600 avoided both the sinter of AuCu/HTs-600 arising from the increased temperature, and the high size of AuNi/HTs-600 resulting from the sinter of single Au nanoparticles at increased temperature. At temperature below 600 °C, dispersion of  $\text{Cu}^{2+}$  and the interaction between  $\text{Cu}^0$  and  $\text{Au}^0$  directed the dispersion of AuCu nanoparticles. At 600 °C, dispersion of  $\text{Ni}^{2+}$  and the interaction between  $\text{Ni}^0$  and AuCu directed the dispersion and inhibited the sinter of AuCu nanoparticles. The low size and narrow distribution of nanoparticles on AuCuNi/HTs-600 proved our deduction.



**Fig. 19** STEM images and metal particle size distributions for AuCuNi/HTs-600 catalyst with different Cu:Ni:Mg:Al atomic ratio. **a** 0.02:0.1:2:1 and **b** 0.05:0.1:2:1

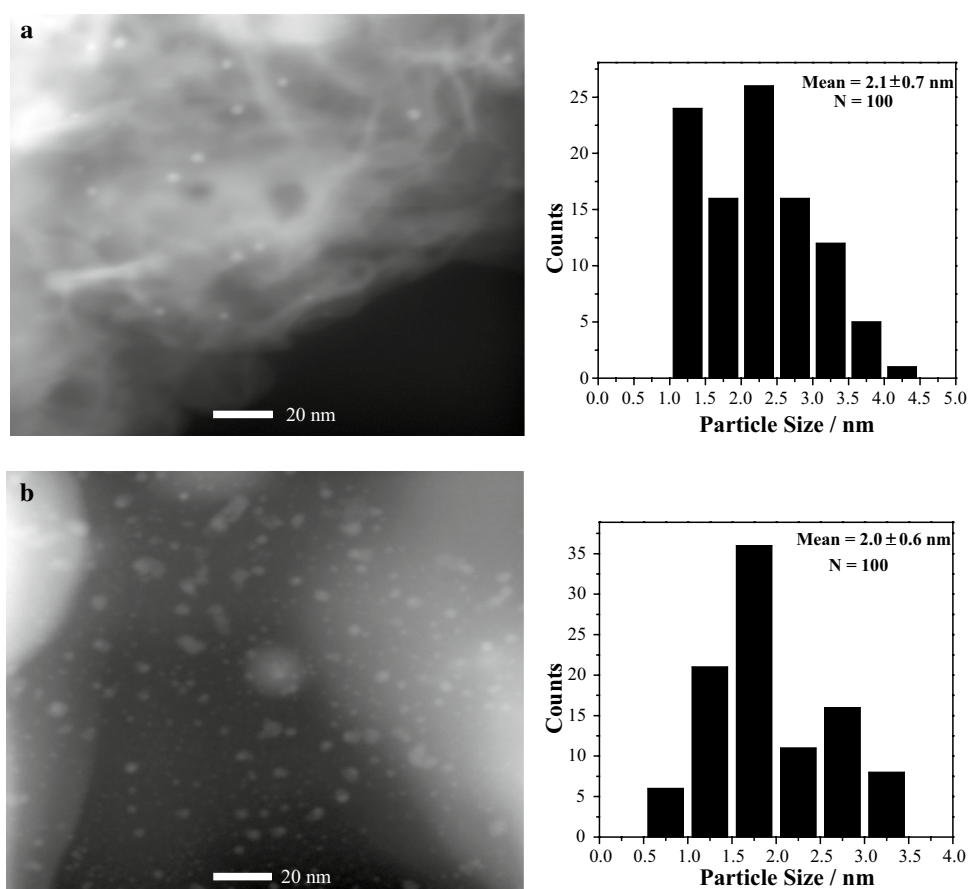


**Table 2** Aerobic oxidation of benzyl alcohol over various catalysts

Entry	Catalysts	Mean size (nm)	Practical metal loading (Au+Cu or Ni) <sup>a</sup>	Benzaldehyde yield <sup>b</sup> (%)	TOF <sup>c</sup> /h <sup>-1</sup>
1	AuCu/HTs-300-C	17.1	0.92 wt% + 3.89 wt%	46	255
2	AuNi/HTs-600-C	9.4	0.88 wt% + 4.02 wt%	33	256
3	AuCu/HTs-300	2.5	0.84 wt% + 3.79 wt%	92	704
4	AuNi/HTs-300	7.8	0.89 wt% + 4.05 wt%	67	398
5	AuNi/HTs-600	6.3	0.91 wt% + 3.92 wt%	85	532
6	AuCuNi/HTs-600	2.0	0.90 wt% + 1.88 wt% + 3.95 wt%	94	684
7	Cu-HTs-300	–		4	–
8	Cu-HTs-600	–		5	–

Reaction conditions: 100 mg catalyst, 1 mmol benzyl alcohol, 8 mL toluene, O<sub>2</sub> bubbling (25–30 mL min<sup>-1</sup>), 100°C, 3 h

<sup>a</sup>Determined by ICP-OES

<sup>b</sup>Yields of benzaldehyde were determined by GC

<sup>c</sup>Turnover frequency=(mole of benzyl alcohol converted after 0.5 h)/(reaction time (0.5 h)×mole of total loading of gold; the amount of catalyst was 0.05 g

### 3.3 Performances of the Bimetal Catalysts in Aerobic Oxidation of Benzyl Alcohol

The catalytic performance of bimetallic catalysts prepared by this work were tested and compared with

those prepared by traditional methods. As shown in Table 2, benzaldehyde yield was below 46% and TOF was <256 h<sup>-1</sup> for bimetallic catalysts prepared by traditional methods in the aerobic oxidation of benzyl alcohol (Entries 1–2). 92% of benzaldehyde yield and TOF

(704 h<sup>-1</sup>) was obtained by AuCu/HTs-300 (Entry 3), which was far higher than that by traditional method. The 704 h<sup>-1</sup> of TOF was also far higher than 400 h<sup>-1</sup> of Au/Cu-HTs in reference [32]. This indicated that the catalysts prepared by this work showed higher activity than those by traditional methods. The benzaldehyde yield by AuNi (i.e., AuNi/HTs-300 and AuNi/HTs-600) was between 67~85% (Entries 4–5), which was higher than that by AuCu/HTs-300-C or AuNi/HTs-600-C (Traditional method) but lower than that by AuCu/HTs-300 (This work). The medium activity of AuNi catalyst was ascribed to its high size. The reason for its high size has been discussed in the previous section. However, the activity of AuCuNi/HTs-600 (Entry 6) was similar with that of AuCu/HTs-300. The high activity of AuCuNi/HTs-600 was also in accordance with the low size of AuCuNi nanoparticles.

The reusability of AuCu/HTs-300 catalysts was also investigated. Table S1 displays the results of recycling experiments of catalysts. The conversions of benzyl alcohol by fresh catalysts were 92%. The conversion decreased from 92% in the first run to 40% in the second run. After second run, the yield did not change apparently. The lower reusability of the catalysts may be due to the leaching of Mg<sup>2+</sup> and the stability of gold particles [42]. In the future work, we will continue to improving our methods to solve this problem.

## 4 Conclusions

In this work, one convenient method was proposed to prepare bimetallic catalysts. The mean size of AuCu/HTs-300 by this new method was 2.5 nm, which was 1/4 (Sequential impregnation) or 1/10 (Co-impregnation) of the size of catalysts by traditional method. Furthermore, the former yield of benzaldehyde was 92%, while the latter was below 46%. The prepared catalysts showed higher activity than that of the catalysts by traditional methods. This demonstrated that the proposed method was successful. In this proposed method, configurational ion Cu<sup>2+</sup> of HTs directed the position and dispersion of the final AuCu nanoparticles on the surface of HTs supports. The direction was realized by employing the interaction between Cu<sup>0</sup> and Au<sup>0</sup>. It was found that dispersion of Cu<sup>2+</sup> (or Ni<sup>2+</sup>) and the interaction between Cu<sup>0</sup> (or Ni<sup>0</sup>) and Au<sup>0</sup> are two key factors affecting the dispersion of AuCu nanoparticles. The dispersion of Cu<sup>2+</sup> (or Ni<sup>2+</sup>) could be controlled by adjusting their contents in HTs supports. The interaction between Cu<sup>0</sup> (or Ni<sup>0</sup>) and Au<sup>0</sup> could be controlled by regulating the reduction temperature. This method could be applied to the controlled synthesis of other bimetallic or trimetallic catalysts.

**Acknowledgements** This work was supported by projects funded by the Major Research Plan of National Natural Science Foundation of China (Program No. 91545130).

## References

- Divins NJ, Angurell I, Escudero C, Pérez-Dieste V, Llorca J (2014) *Science* 346:620–623
- Bracey CL, Ellis PR, Hutchings GJ (2009) *Chem Soc Rev* 38:2231–2243
- Baldizzone C, Mezzavilla S, Carvalho HWP, Meier JC, Schuppert AK, Heggen M, Galeano C, Grunwaldt J, Schüth F, Mayrhofer KJJ (2014) *Angew Chem Int Ed* 53:14250–14254
- Paalanen P, Weckhuysen BM, Sankar M (2013) *Catal Sci Technol* 3:2869–2880
- Fang W, Chen J, Zhang Q, Deng W, Wang Y (2011) *Chem Eur J* 17:1247–1256
- Liu X, Wang A, Yang X, Zhang T, Mou C, Su D, Li J (2008) *Chem Mater* 21:410–418
- Falsig H, Hvolbæk B, Kristensen IS, Jiang T, Bligaard T, Christensen CH, Nørskov JK (2008) *Angew Chem* 120:4913–4917
- Li L, Gao Y, Li H, Zhao Y, Pei Y, Chen Z, Zeng X (2013) *J Am Chem Soc* 135:19336–19346
- Liao F, Lo TWB, Tsang SCE (2015) *ChemCatChem* 7:1998–2014
- Bauer JC, Mullins D, Li M, Wu Z, Payzant EA, Overbury SH, Dai S (2011) *Phys Chem Chem Phys* 13:2571–2581
- Lu J, Low KB, Lei Y, Libera JA, Nicholls A, Stair PC, Elam JW (2014) *Nat Commun* 5:3264–3272
- Zhong R, Sun K, Hong Y, Xu B (2014) *ACS Catal* 4:3982–3993
- Rebelli J, Detwiler M, Ma S, Williams CT, Monnier JR (2010) *J Catal* 270:224–233
- Barbier J, In: Ertl G, Knözinger H, Weitkamp J (Eds) (1999) *Preparation of solid catalysts*, Wiley-VCH Verlag GmbH
- Lamy-Pitara E, Ouazzani-Benhima LEI, Barbier J (1992) *Appl Catal A* 81:47–65
- Pieck CL, Marecot P, Barbier J (1996) *Appl Catal A* 143:283–298
- Barbier J, Marécot P, Del Angel G, Bosch P, Boitiaux JP, Didillon B, Dominguez JM, Schifter I, Espmosa G (1994) *Appl Catal A* 116:179–186
- Rebelli J, Rodriguez AA, Ma S, Williams CT, Monnier JR (2011) *Catal Today* 160:170–178
- Beard KD, Borrelli D, Cramer AM, Blom D, Van Zee JW, Monnier JR (2009) *ACS Nano* 3:2841–2853
- Ohashi M, Beard KD, Ma S, Blom DA, St-Pierre J, Van Zee JW, Monnier JR (2010) *Electrochim Acta* 55:7376–7384
- Beard KD, Van Zee JW, Monnier JR (2009) *Appl Catal B* 88:185–193
- Rodriguez AA, Williams CT, Monnier JR (2014) *Appl Catal A* 475:161–168
- Jia Q, Zhao D, Tang B, Zhao N, Li H, Sang Y, Bao N, Zhang X, Xu X, Liu H (2014) *J Mater Chem A* 2:16292–16298
- Guan Y, Zhao N, Tang B, Jia Q, Xu X, Liu H, Boughton RI (2013) *Chem Commun* 49:11524–11526
- Hakim SH, Sener C, Alba-Rubio AC, Gostanian TM, O'Neill BJ, Ribeiro FH, Miller JT, Dumesic JA (2015) *J Catal* 328: 75–90
- Wang H, Liu D, Xu C (2016) *Catal Sci Technol* 6:7137–7150
- Liu P, Degirmenci V, Hensen EJM (2014) *J Catal* 313: 80–91
- Debecker DP, Gaigneaux EM, Busca G (2009) *Chem Eur J* 15:3920–3935
- Xu Z, Zhang J, Adebajo MO, Zhang H, Zhou C (2011) *Appl Clay Sci* 53:139–150

30. Fan G, Li F, Evans DG, Duan X (2014) *Chem Soc Rev* 43:7040–7066
31. Zope BN, Hibbitts DD, Neurock M, Davis RJ (2010) *Science* 330:74–78
32. Liu P, Guan Y, Santen RA, Li C, Hensen EJM (2011) *Chem Commun* 47:11540–11542
33. Wang J, Lang X, Zhaorigetu B, Jia M, Wang J, Guo X, Zhao J (2014) *ChemCatChem* 6:1737–1747
34. Zhao J, Yu G, Xin K, Li L, Fu T, Cui Y, Liu H, Xue N, Peng L, Ding W (2014) *Appl Catal A* 482:294–299
35. Du Y, Jin Q, Feng J, Zhang N, He Y, Li D (2015) *Catal Sci Technol* 5:3216–3225
36. Xu C, Sun J, Zhao B, Liu Q (2010) *Appl Catal B* 99:111–117
37. Liu P, Derchi M, Hensen EJM (2014) *Appl Catal B* 144:135–143
38. Pojanavaraphan C, Luengnaruemitchai A, Gulari E (2013) *Appl Catal A* 456:135–143
39. Luo M, Bian P, Zheng X (1998) *Chin J Appl Chem* 15:113–114
40. Liu J, Qiao B, Song Y, Huang Y, Liu J (2015) *Chem Commun* 51:15332–15335
41. Kirkemide A, Spurlin S, Draxler-Sixta L, Cooper J, Ren S (2015) *Angew Chem Int Ed* 54:4203–4207
42. Wang Z, Xu C, Wang H (2014) *Catal Lett* 144:1919–1929